PHYSICAL REVIEW B **108**, 144413 (2023)

Benchmarking density functional theory on the prediction of antiferromagnetic transition temperatures

Zahra Mosleh [*] and Mojtaba Alaei [†]
Department of Physics, Isfahan University of Technology, Isfahan 84156-83111, Iran

(Received 9 August 2023; accepted 29 September 2023; published 16 October 2023)

This study investigates the predictive capabilities of common density functional theory (DFT) methods (GGA, GGA+U, and GGA+U+V) for determining the transition temperature of antiferromagnetic insulators. We utilize a data set of 29 compounds and derive Heisenberg exchanges based on DFT total energies of different magnetic configurations. To obtain exchange parameters within a supercell, we have devised an innovative method that utilizes null-space analysis to identify and address the limitations imposed by the supercell on these exchange parameters. With obtained exchanges, we construct Heisenberg Hamiltonian to compute transition temperatures using classical Monte Carlo simulations. To refine the calculations, we apply linear response theory to compute onsite (U) and intersite (V) corrections through a self-consistent process. Our findings reveal that GGA significantly overestimates the transition temperature (by 113%), while GGA+U underestimates it (by 53%). To improve GGA+U results, we propose adjusting the DFT results with the $(S+1)/S$ coefficient to compensate for quantum effects in Monte Carlo simulation, resulting in a reduced error of 44%. Additionally, we discover a high Pearson correlation coefficient of approximately 0.92 between the transition temperatures calculated using the GGA+U method and the experimentally determined transition temperatures. Furthermore, we explore the impact of geometry optimization on a subset of samples. Using consistent structures with GGA+U and GGA+U+V theories reduced the error.

DOI: 10.1103/PhysRevB.108.144413

I. INTRODUCTION

Magnetic materials find numerous applications, ranging from energy harvesting to computer memories [1–3]. The key to utilizing these materials effectively lies in understanding their magnetic order and transition temperature, as these properties determine their potential applications. Determining these properties requires expensive experiments like neutron diffraction [4], which can be impractical for all compounds created in labs. Therefore, there is a growing need for reliable and computationally efficient *ab initio* methods to accurately predict magnetic order and transition temperature.

Additionally, computational material scientists have gained the ability to simulate numerous nonexistent materials using a combination of *ab initio* methods, like density functional theory (DFT), and advanced techniques such as machine learning and evolutionary algorithms [5]. The accurate prediction of magnetic properties for these materials is essential to discover new magnetic substances with desirable characteristics [6]. This significance is particularly pronounced for magnetic materials, as there is a pressing need for expanded databases to explore and identify novel materials using machine-learning approaches effectively.

Theoretical predictions of material properties, including thermodynamics, can be obtained from quantum *ab initio* calculations. However, these calculations are computationally expensive, making them feasible primarily at zero temperature. To address this issue, various strategies have been developed. One practical approach involves mapping essential material features onto a simpler physical model. In the context of magnetic materials and magnetic energy models, a key feature is the magnetic interactions between atomic magnetic moments such as Heisenberg exchanges. The strength of these interactions can be determined through *ab initio* calculations using different strategies. Subsequently, these interactions are used to construct a magnetic model. To obtain macroscopic properties, such as thermodynamic properties like phase transition temperature and Curie-Weiss temperature of the magnetic material, classical spin Monte Carlo (MC) simulations are employed for the magnetic model.

Most magnetic materials contain atoms with d or f orbitals in their valence states, resulting in strong electron-electron correlations that pose challenges for most *ab initio* methods. Some sophisticated techniques, such as dynamical mean-field theory (DMFT) [7] and continuum quantum Monte Carlo [8,9], can address these challenges with a high level of accuracy. However, these methods are computationally expensive and practical only in specific cases. A more practical and cost-effective solution to improve electron-electron interactions in DFT is to incorporate the Hubbard correction, known as DFT+U [10–12]. The Hubbard U parameter serves as a regulatory factor and can be estimated using various approaches, such as linear response theory.

This paper presents a systematic study focused on assessing the effectiveness of linear response theory in predicting appropriate U parameters for accurately calculating magnetic

---

[*] z.mosleh@ph.iut.ac.ir

[†] m.alaei@iut.ac.ir

interactions in insulating antiferromagnetic materials. To do this, we specifically select magnetic materials for which experimental data, such as phase transition temperature, are available. Additionally, we explore the effects of geometrical optimization and the calculation of U through a self-consistent process. To derive thermodynamic properties, we employ Monte Carlo simulations (MC) based on magnetic interactions obtained from DFT+U calculations. Finally, we assess the accuracy of the U parameters by comparing transition temperatures obtained through MC simulations with experimental data. Along with the DFT+U benchmark, we provide a benchmark for generalized gradient approximation (GGA) of exchange-correlation functional in DFT in predicting transition temperature.

II. MATERIALS AND COMPUTATIONAL METHODS

A. Materials

In this study, we choose 29 different antiferromagnetic crystals, from well-known transition monoxides such as MnO and NiO to complicated compounds such as $LiMnPO_4$. We try to have a variety of crystal symmetries in our choice. We restrict our selections among materials with $3d$ valence magnetic atoms to avoid spin-orbit effects. Because DFT, i.e., GGA and local density approximation (LDA), underestimates the magnetic moment of some itinerant magnetic materials [13], we limit the candidate to only insulator antiferromagnetic systems. The chemical formulas of our compounds are as follows: $BiFeO_3$ [14], $CoWO_4$ [15], Cr_2O_3 [16], Cr_2TeO_6 [17], Cr_2WO_6 [17], $CrCl_2$ [18], Fe_2O_3 [19], Fe_2TeO_6 [17], KMnSb [20], $KNiPO_4$ [21], La_2NiO_4 [22], $LaFeO_3$ [23], Li_2MnO_3 [24], $LiCoPO_4$ [25], $LiMnO_2$ [26], $LiMnPO_4$ [27], $LiNiPO_4$ [28], MnF_2 [29], MnO [30], MnS [31], MnSe [32], MnTe [33], $MnWO_4$ [34], $NiBr_2$ [35], NiF_2 [36], NiO [30], $NiWO_4$ [37],$YFeO_3$ [38], and YVO_3 [39].

B. Computational methods

1. Ab initio computational details

The total energy calculations are performed using density functional theory in two different codes: the plane-wave pseudopotential QUANTUM ESPRESSO (QE) package [40] and the full-potential local-orbital (FPLO) code [41]. In QE, we utilize GBRV ultrasoft pseudopotentials [42]. We use the experimental crystal structure parameters for all cases. We adopt the generalized gradient approximation (GGA) in the Perdew-Burke-Ernzerhoff form (PBE) for the exchange-correlation potential. To expand the wave function and charge density in the plane wave, we set 40 and 400 Ry cutoffs for all compounds, respectively. To sample the Brillouin zone (BZ), we employ the Monkhorst-Pack scheme [43] with a mesh spacing of 0.2 $\frac{1}{A^\circ}$.

Due to the known underestimation of electron-electron Coulomb interactions in GGA, we apply the Hubbard U correction method, commonly called GGA+U (or LDA+U). We estimate the self-consistent Hubbard U parameter with a precision of about 0.01 eV using linear response theory [44] through density functional perturbation theory (DFPT) [45,46].

We employ the Bader charge analysis code [47–50] for charge distribution, magnetic moment analysis, and determining the percentage of atoms ionizations in each compound.

2. Deriving Heisenberg exchange parameters

To obtain Heisenberg exchange interactions, we map the spin-polarized DFT total energy of different magnetic configurations into the following Heisenberg Hamiltonian:

$$H = -\frac{1}{2}\sum_{i,j} J_{ij}\hat{S}_i \cdot \hat{S}_j, \tag{1}$$

where J_{ij} indicates the strength of Heisenberg exchange interaction (Heisenberg exchange parameters) between ith and jth sites, and $\hat{S}_i$ denotes the unit vector of magnetic moment direction on the lattice site i. We need only consider the collinear spin configurations to derive the Heisenberg exchange. So instead of assigning the direction of the magnetic moment by vectors, we only need to assign them by ±1 (i.e., $\hat{S}_i = \pm 1$).

To calculate the exchange parameters up to the nth nearest neighbor, the distance of the nth nearest neighbor should fit within the crystal cell. Therefore, we extend the primitive cell to an appropriate supercell for this purpose. However, determining the farthest neighbor for which we can calculate the exchange parameter should not solely rely on comparing the distance of neighbors and the size of the supercell. An additional criterion must be considered due to the periodic boundary conditions. Below, we elaborate on this crucial criterion.

Given a magnetic configuration, for instance, the kth configuration, where the magnetic moment directions are specified with specific values (e.g., $\hat{S}_1 = 1$, $\hat{S}_2 = -1$, $\hat{S}_3 = -1$, and so on), the Heisenberg Hamiltonian for this configuration can be expressed as follows:

$$E_k = \sum_{i}^{m} \alpha_{ki} J_i + c. \tag{2}$$

In this equation, E_k represents the total energy of the kth magnetic configuration obtained from DFT, J_i denotes the Heisenberg exchange parameter for the ith nearest neighbor, c is a constant, and α_{ki} indicates the coefficient corresponding to the ith nearest neighbor for this particular configuration. The values of α_{ki} are determined by the specific magnetic moment directions (e.g., $\hat{S}_1$, $\hat{S}_2$, $\hat{S}_3$, and so on) for the kth configuration. Each magnetic configuration (e.g., k) will have its set of coefficients α_{ki} corresponding to the different nearest neighbors, leading to a matrix of coefficients. Analyzing the null space [51] of this coefficient matrix can provide insights into the dependencies between the coefficients for different nearest neighbors, allowing us to determine the farthest neighbor for which we are permitted to calculate the Heisenberg exchange parameters. We explain this analysis in more detail in Appendix B.

To obtain the Heisenberg exchanges up to the nth nearest neighbor, theoretically, we only need a minimum of $n + 1$ distinct magnetic configurations. However, in practice, additional complexity arises from the induced magnetic moments of anions, such as oxygen atoms. Consequently, using more magnetic configurations and determining the Heisenberg exchanges through the least-squares method is advisable, as recommended in our previous work [52]. Therefore, to account for these additional complexities and ensure more accurate results, we use a number of magnetic configurations around three times greater than the minimum required number.

3. *Monte Carlo simulation*

To calculate the antiferromagnetic transition temperature (i.e., Néel temperature) of all compounds, we perform classical Monte Carlo (MC) simulations using the replica exchange method as implemented in the Esfahan spin simulation package (ESpinS) as an open-source classical spin MC software package [53]. We choose the supercell for each compound in a way that the supercell contains around 2000 sites. For each replica, at each temperature, 5×10^5 Monte Carlo steps (MCs) per spin are considered for the thermal equilibrium and data collection, respectively. Measurements are done after skipping every 5 MCs to lower the correlation between the data.

III. RESULTS AND DISCUSSION

A. Accuracy of GBRV pseudopotentials for Heisenberg exchanges

One of the critical aspects in *ab initio* calculations is the reliability of pseudopotentials, especially when dealing with 3*d* transition metals. This is particularly crucial due to the impact of semicore states and the highly localized nature of 3*d* electrons [54,55]. While GBRV pseudopotentials have been thoroughly examined, their accuracy in predicting Heisenberg exchange interactions lacks a benchmark. To address this, we conduct a comparison between full-potential FPLO results and QE GBRV pseudopotentials within the GGA exchange-correlation functional. For this comparison, we use 12 different magnetic configurations for each compound. Figure 1 indicates the strongest antiferromagnetic exchange values for both FPLO and GBRV. Notably, there is a high degree of consistency between the all-electron FPLO and GBRV/QE methods, with an average difference of around 1.4 meV. Further detailed results can be found in Tables S1, S2, S3, and S4 of the Supplemental Material [56].

B. Transition temperatures

To predict the transition temperatures for all samples, we employ the Heisenberg exchange parameters obtained from both GGA and GGA+U calculations. We use these parameters in Monte Carlo (MC) simulations, which allow us to determine the transition temperatures based on the peak of the magnetic-specific heat. In the Supplemental Material [56], we provide comprehensive details of the Heisenberg exchange parameters and transition temperatures in Tables S5, S6, S7, and S8 for all compounds using both GGA and GGA+U methods. Figure 2 presents a comparison between the experimental transition temperatures $T_C^{\text{Expt.}}$ (depicted by the solid line) and the results obtained from GGA and GGA+U calculations, indicating with T_C^{MC} axis. The GGA method significantly overestimates the transition temperatures, with a mean absolute percentage error (MAPE) of 113%. However, in three cases (La$_2$NiO$_4$, LaFeO$_3$, and YFeO$_3$), GGA underestimates the transition temperature. On the other hand, the GGA+U approach generally underestimates transition temperatures, except for three compounds (Fe$_2$TeO$_6$, Li$_2$MnO$_3$,

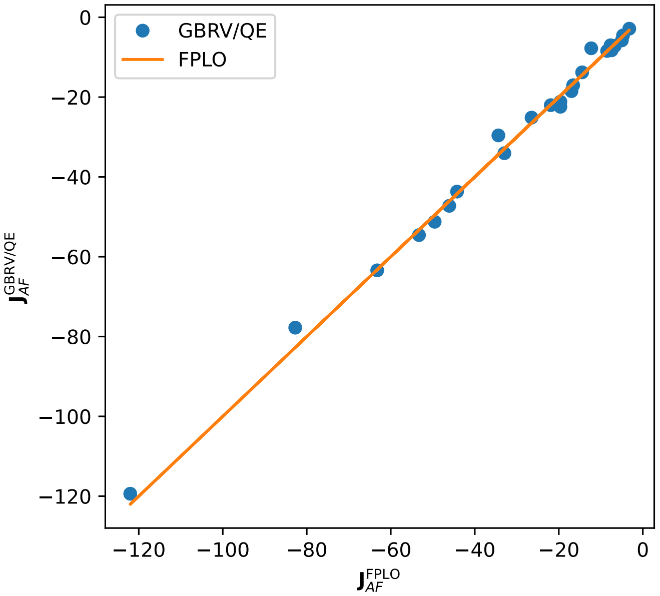

FIG. 1. Comparison between full-potential method using FPLO code and GBRV pseudopotentials using QE code. We plot strongest antiferromagnetic exchange for FPLO and GBRV. The line and circles indicate FPLO and QE results, respectively. In the plot, the results of La2NiO4, LiCoPO4, and CoWO4 are absent since FPLO calculations for some of the magnetic configurations of these compounds do not converge.

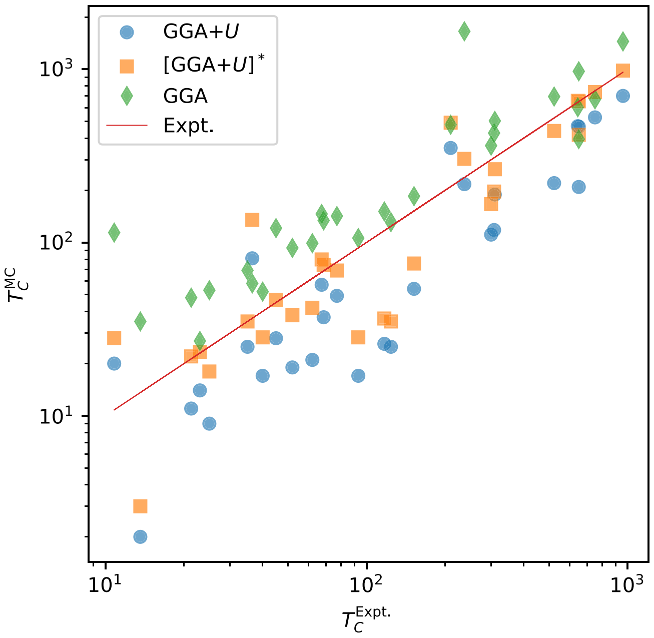

FIG. 2. The plot compares the experimental transition temperature of 29 compounds with GGA and GGA+U. We compute the transition temperatures for GGA and GGA+U using Monte Carlo simulation. The [GGA+U]* data show implementing $(S+1)/S$ correction to GGA+U.

TABLE I. The table shows transition temperatures for a subset of samples, with and without geometry optimization. T_U and T_{UV} represent the transition temperatures (Néel temperatures) obtained using the GGA+U and GGA+U+V calculations without geometry optimization, respectively. The Hubbard parameters U and V (onsite U and intersite V) are obtained from self-consistent linear response theory calculations. On the other hand, T_U^{opt} and T_{UV}^{opt} indicate Néel temperatures obtained from GGA+U and GGA+U+V calculations through geometry optimization along with self-consistent linear response theory calculations for computing U and V. The values inside parentheses indicate the temperatures after applying the $\frac{S+1}{S}$ correction factor. The last column presents the experimental temperature value documented in the literature.

Sample	S	T_U (K)	T_{UV} (K)	T_U^{opt} (K)	T_{UV}^{opt} (K)	$T_{\text{Expt.}}$ (K)
NiO	1	220 (440)	246 (492)	210 (420)	236 (472)	523 [62]
MnO	$\frac{5}{2}$	27 (37.8)	43 (60.2)	72 (100.8)	87 (121.8)	117 [63]
MnS	$\frac{5}{2}$	54 (75.6)	60 (84.0)	58 (81.2)	65 (91.0)	152 [31]
MnSe	$\frac{5}{2}$	25 (35)	26 (36.4)	37 (51.8)	44 (61.6)	124 [64]
NiF_2	1	37 (74)	44 (88)	32 (64)	40.2 (80.4)	68.5 [65]
MnF_2	$\frac{5}{2}$	57 (79.8)	67 (93.8)	44 (61.6)	57 (79.8)	67.3 [66]
MnTe	$\frac{5}{2}$	189 (264.6)	196 (274.4)	152 (212.8)	156 (218.4)	310 [67]
$CrCl_2$	2	2 (3)	2 (3)	19 (28.5)	16 (24.0)	11.3–16 [68]
MAPE		58% (41%)	52% (41%)	51% (37%)	41% (31%)	

and $MnWO_4$) where they are overestimated. The GGA+U method reduces the MAPE in estimating transition temperatures to 53%. Despite these errors, We observe Pearson correlation coefficients of 0.74 and 0.92 for the transition temperatures of GGA and GGA+U, respectively, when compared to the experimental values. These findings can be valuable for future research, especially in the context of machine-learning applications.

Due to the classical nature of our MC simulations, in our previous work [52], we introduced a correction factor of $(S+1)/S$ as follows:

$$T_C^{\text{MC}*} = \frac{S+1}{S} T_C^{\text{MC}}. \tag{3}$$

Here, S represents the nominal spin magnetic moment for the ionic magnetic atom in each compound. We represent this corrected approach in the figure as [GGA+U]*. By applying this correction, the MAPE is further reduced to 44%, significantly improving the accuracy of our transition temperature predictions. In [GGA+U]*, 45% of compounds have absolute percentage error (APE) less than 20%, 25% of compounds have APE between 20% and 40%, and 20% compounds have APE between 40% and 80%. There are three compounds (i.e., Fe_2TeO_6, Li_2MnO_3, and $MnWO_4$) that have APE larger than 100%. The worst case is Li_2MnO_3 (with 270 APE), where GGA+U predicts the compound as ferromagnet while the experiment indicates an antiferromagnetic ground state for the compound [57]. The other *ab initio* calculation based on DFT+U also wrongly predicts this material as a ferromagnet [58]. This is because of bad overestimation of Hubbard U for this compound. Our investigation finds that the U parameter should be less than 2.01 eV for this compound to have an antiferromagnetic ground state. In comparison, the self-consistent linear response method overestimates it as 6.39 eV.

On average, according to our data, self-consistent Hubbard U is 0.5 eV smaller than the non-self-consistent Hubbard U. Since larger Hubbard U decreases the antiferromagnetic interaction, and in GGA+U for most cases, there is an underestimation of antiferromagnetic interactions, estimation of Hubbard U through the self-consistent process is vital to predicting the transition temperature.

Although [GGA+U]* produces reasonably accurate results for approximately 50% of cases, it also exhibits significant errors in some instances. To better understand the reasons behind these discrepancies, we conducted an analysis to investigate whether there exists any meaningful correlation between the APE of [GGA+U]* and various compound properties, such as the magnetic moment. To do this, we considered several properties, including the Shannon entropy of d orbital in density of states (DOS), the distance between the center of d orbital, and the center of p orbital in DOS, band gap, magnetic moment, ionic bond percentage, total stress, and force. Detailed information on these properties for each compound can be found in Tables II and III in Appendix A. The results of our analysis indicate that there is no meaningful correlation between these properties and the APE of the transition temperature derived from [GGA+U]*.

We also investigate the extended Hubbard model, so-called GGA+U+V [59–61] containing both onsite (U) and intersite electronic interactions (V), on only 18 compounds. If we still consider the $(S+1)/S$ correction for analysis of GGA+U+V results, there is no critical gain for transition temperature compared to GGA+U, on average. The results of GGA+U and GGA+U+V on the prediction of transition temperatures are collected in Tables IV and V of Appendix C.

Ultimately, we explore the effect of geometry optimization of primitive antiferromagnetic cells (atomic positions and crystal lattice vectors) to determine if the consistent crystal structures with GGA+U and GGA+U+V lead to more corrected results for transition temperature. For this purpose, we choose eight compounds with low computational cost, then optimize their structures and then recalculate U and V parameters for the optimized structures. We repeat this procedure until we reach optimized structures with self-consistent U and V parameters. We collect the results in Table I with $(S+1)/S$ correction inside the parentheses. Without geometry optimization and considering $(S+1)/S$ correction, GGA+U and

GGA+U+V have almost similar results. Both GGA+U and GGA+U+V for these eight compounds (using self-consistent U and V) indicate 41% MAPE for predicting transition temperatures, comparable with MAPE obtained for all 29 compounds. Using optimized structures decrees MAPE to 37% and 31% for GGA+U and GGA+U+V (with $(S+1)/S$ correction), respectively. Therefore, consistent structures with GGA+U and GGA+U+V theories can be beneficial for better prediction.

IV. CONCLUSIONS

The study conducted systematic research to benchmark three different density functional theory (DFT) methods, GGA, GGA+U, and GGA+U+V, for predicting transition temperatures in a group of antiferromagnetic insulators. The results indicate that obtaining Hubbard U parameters through self-consistent processes using linear response theory is crucial for accurate predictions. Additionally, optimizing the structures of the materials leads to more consistent outcomes with experimental data. To enhance the accuracy of GGA+U results, the study recommends applying a $(S+1)/S$ correction to the GGA+U approach. Moreover, the work introduces a method to determine the appropriate number of nearest neighbors to calculate exchanges within a supercell. In conclusion, this study highlights the performance of various DFT methods in predicting transition temperatures for antiferromagnetic insulators. It also proposes correction strategies to improve the accuracy of these predictions, providing valuable insights for future research in this area.

ACKNOWLEDGMENTS

The authors thank I. Timrov for helping them with GGA+U and GGA+U+V calculations. M.A. thanks M. Gazor for introducing the null-space concept in linear algebra and F. Shahbazi for suggesting the Shannon entropy to measure the localization of d orbitals in DOS.

APPENDIX A: CHARACTERIZATION OF COMPOUNDS

1. Hubbard parameter

The Hubbard U parameters are determined using linear response density-functional perturbation theory (LR-DFPT). Typically, the U value is computed with a precision of approximately 0.01 eV, and this calculation is carried out iteratively until convergence is achieved. The calculated U parameters for various compounds are summarized in Table II.

TABLE II. Hubbard parameter, magnetic moment, total stress, total force, ionic percentage, and charge distribution for all samples within GGA+U approximation. The data inside the parentheses represent the calculated magnetic moment and ionic percentage in the GGA approach.

Sample	Hubbard parameter (eV)	Magnetic moment (μ_B)	Total stress $\left(\frac{Ry}{bohr^3}\right)$	Total force $\left(\frac{Ry}{bohr}\right)$	Ionic percentage	Charge distribution
NiO	7.17	1.72(1.33)	104.84	0	63(56)	$Ni^{+1.26}$ $O^{-1.25}$
MnO	4.81	4.61(4.40)	84.99	0	72.5(69.5)	$Mn^{+1.45}$ $O^{-1.44}$
MnS	4.39	4.61(4.33)	30.63	0	63(58.5)	$Mn^{+1.26}$ $S^{-1.25}$
MnSe	4.19	4.62(4.35)	30.31	0	57.5(52.5)	$Mn^{+1.15}$ $Se^{-1.14}$
Cr_2O_3	5.93	2.88(2.63)	152.96	0.033	62.3(58)	$Cr^{+1.85}$ $O^{-1.23}$
Fe_2O_3	6.18	4.25(3.40)	219.66	0.316	61.6(52.6)	$Fe^{+1.86}$ $O^{-1.24}$
$BiFeO_3$	6.13	4.25(3.81)	23.05	0.027	62.3(55)	$Bi^{+1.86}$ $Fe^{+1.87}O^{-1.24}$
$NiBr_2$	6.31	1.66(1.39)	1.34	0.001	46.5(38.5)	$Ni^{+0.93}$ $Br^{-0.46}$
YVO_3	4.74	1.81(1.55)	81.33	0.037	64(60)	$Y^{+2.16}$ $V^{+1.92}O^{-1.36}$
$LiMnPO_4$	4.20	4.68(4.58)	55.56	0.252	78.5(75.5)	$Li^{+0.9}$ $Mn^{+1.57}P^{+4.88}O^{-1.7}$
$LiNiPO_4$	7.22	1.80(1.58)	75.45	0.128	69(63)	$Li^{+0.9}$ $Ni^{+1.38}P^{+4.88}O^{-1.83}$
$LiCoPO_4$	5.91	2.78(2.60)	54.93	0.053	72(67)	$Li^{+0.9}$ $Co^{+1.44}P^{+4.88}O^{-1.84}$
$YFeO_3$	6.22	4.23(3.79)	76.98	0.028	62(55)	$Y^{+2.17}$ $Fe^{+1.86}O^{-1.34}$
$LaFeO_3$	6.26	4.22(3.77)	76	0.145	61.6(55)	$La^{+2.09}$ $Fe^{+1.85}O^{-1.31}$
$LiMnO_2$	5.97	3.92(3.55)	101.46	0.070	56.6(53)	$Li^{+0.89}$ $Mn^{+1.70}O^{-1.31}$
$CrCl_2$	6.41	3.84(3.69)	41.43	0.018	69.5(63.53)	$Cr^{+1.39}$ $Cl^{-0.70}$
$KNiPO_4$	7.13	1.81(1.59)	56.18	0.259	67.5(60.5)	$K^{+0.87}$ $Ni^{+1.35}P^{+4.88}O^{-1.79}$
MnF_2	3.84	4.68(4.59)	56.13	0.002	80.5(78.5)	$Mn^{+1.60}$ $F^{-0.80}$
NiF_2	7.14	1.81(1.62)	55.76	0.006	75(69.5)	$Ni^{+1.50}$ $F^{-0.74}$
Fe_2TeO_6	6.12	4.31(3.87)	175.19	0.093	65(58.3)	$Fe^{+1.95}$ $Te^{+5.92}$ $O^{-1.65}$
La_2NiO_4	7.58	1.76(0.55)	77.46	0.030	66.5(55.5)	$La^{+2.01}$ $Ni^{+1.33}$ $O^{-1.34}$
Cr_2TeO_6	5.89	2.87(2.64)	223.71	0.234	64(59.6)	$Cr^{+1.92}$ $Te^{+5.9}$ $O^{-1.64}$
KMnSb	4.33	4.70(4.20)	29.83	0.032	34(26.5)	$K^{+0.72}$ $Mn^{+0.68}$ $Sb^{-1.39}$
Cr_2WO_6	6.01	2.89(2.66)	114.6	0.042	65.3(61.6)	$Cr^{+1.96}$ $W^{+3.10}$ $O^{-1.18}$
$NiWO_4$	7.74	1.84(1.52)	61.22	0.109	72.5(65)	$Ni^{+1.45}$ $W^{+2.99}$ $O^{-1.15}$
$MnWO_4$	5.71	4.61(4.36)	92.63	0.217	81(79.5)	$Mn^{+1.62}$ $W^{+2.99}$ $O^{-1.16}$
$CoWO_4$	6.53	2.78(2.57)	100.78	0.080	73(69.5)	$Co^{+1.46}$ $W^{+3.02}$ $O^{-1.16}$
Li_2MnO_3	6.39	3.27(2.68)	87.54	0.065	47.5(45.2)	$Li^{+0.88}$ $Mn^{+1.90}$ $O^{-1.24}$
MnTe	4.05	4.63(4.28)	26.42	0	47.5(41.5)	$Mn^{+0.95}$ $Te^{-0.96}$

2. Ionic percentage and magnetic moment

To describe the covalent and ionic nature of bonds, the net charges of ions are calculated using Bader charge analysis [69] using BADER code [70]. The results evident that net charge on atoms in compounds are less than nominal charges. For example, in NiO about 1.26 electrons transfer from each Ni atom to O atoms while nominal charges are +2 for Ni and −2 for O ions. Therefore, in NiO, the bond between Ni and O atom shows obvious ionic character and a little covalent bond (37%). The ionic percentage of different compounds is shown in Table II. The results reveal that in all compounds, the bonding behavior consists of a combination of ionic and covalent bonds. When comparing the results obtained from GGA and GGA+U calculations, it becomes evident that the degree of ionic bonding increases across all compounds when using the GGA+U approach. This increase in ionic character is a result of correcting the onsite Coulomb interaction, which aligns with the findings in Ref. [71].

We also determine the magnetic moment through Bader charge analysis, using two different approximations: GGA and GGA+U. Notably, the magnetic moment exhibits an increase when employing the GGA+U approximation, as depicted in Table II. This phenomenon can be attributed to the relationship between the magnetic moments of the transition metal atoms and their localized d electron shells. The GGA+U approximation increases d electron shells localization and eliminates fractional occupation numbers, which is why we anticipate an increase in the magnetic moment when utilizing this approach [72].

3. Projected density of states and band gap

We present the project density of states (PDOS) for all compounds in Figs. S1 and S2 of the Supplemental Material [56] using GGA+U approximation. To convert PDOS information to numbers, we define Shannon entropy to measure the localization of the d orbital of magnetic atoms in energy space:

$$S^d_{\mathrm{PDOS}} = -\sum_{E<E_{\mathrm{Fermi}}} \rho_d(E) \ln \rho_d(E). \tag{A1}$$

Here, $\rho_d(E)$ is the normalized DOS of d orbitals of magnetic atoms, and E_{Fermi} is Fermi level energy. Additionally, we calculate the distance between the center of d orbitals of magnetic moment and the p orbitals of anions in the energy space (d-p distance) to give a measure of the separation of these orbitals. This information is gathered in Table III.

We also report the band gap obtained from the GGA+U calculation in Table III. We add to the table the existing gap reported in the experiments. The gap error using GGA+U for these materials, on average, is about 30%. For some materials, GGA+U overestimates the gap, and for others underestimates the gap in comparison with the experiment (Fig. 3).

TABLE III. The Shannon entropy of d orbitals (S^d_{PDOS}) defined in Eq. (A1) obtained from PDOS, the distance between p orbital center and d orbital center (d-p distance), GGA+U band gap $E_g^{\mathrm{GGA}+U}$ for all samples, and the reported experimental value of the band gap $E_g^{\mathrm{Expt.}}$.

Sample	S^d_{PDOS}	d-p distance (eV)	$E_g^{\mathrm{GGA}+U}$ (eV)	$E_g^{\mathrm{Expt.}}$ (eV)
NiO	4.05	0.82	3.2	4.0 [73]
MnO	3.96	0.25	1.9	3.9 [73]
MnS	3.44	1.08“	2.3	2.7–2.8 [74]
MnSe	3.14	1.39	1.4	2–2.5 [74]
Cr_2O_3	4.08	0.80	3.9	3.1 [75]
Fe_2O_3	3.70	3.26	1.9	2.6 [76]
$BiFeO_3$	2.92	3.66	2.7	2.1 [77]
$NiBr_2$	3.39	2.85	2.5	
YVO_3	4.02	1.05	2.8	
$LiMnPO_4$	3.97	0.68	4.1	3.8–4.0 [78]
$LiNiPO_4$	4.05	1.28	4.7	
$LiCoPO_4$	4.18	0.38	4.5	
$YFeO_3$	3.08	2.96	3.2	2.46 [79]
$LaFeO_3$	3.08	0.36	3.0	2.65 [80]
$LiMnO_2$	4.13	1.42	1.3	0.79 [81]
$CrCl_2$	3.70	0.56	3.8	
$KNiPO_4$	3.92	0.14	3.8	
MnF_2	3.61	1.36	3.6	
NiF_2	4.01	1.00	5.4	8.07 [82]
Fe_2TeO_6	3.50	3.32	1.8	1.46 [83]
La_2NiO_4	4.22	2.06	0.3	1.51 [84]
Cr_2TeO_6	4.17	0.18	2.5	
KMnSb	2.29	3.35	1.2	
Cr_2WO_6	4.21	1.45	2.0	
$NiWO_4$	4.13	1.73	2.9	3.4–3.6 [85]
$MnWO_4$	4.17	1.00	2.5	2.7 [86]
$CoWO_4$	4.20	1.34	3.2	2.25 [87]
Li_2MnO_3	3.33	2.40	2.1	1.76 [88]
MnTe	2.75	1.84	0.7	0.9–1.3 [74]
MAPE			30%	

APPENDIX B: NULL-SPACE ANALYSIS

Figure 4 illustrates the calculation of Heisenberg exchange parameters using the DFT total energy of different configurations within a supercell. In this method, for each magnetic configuration, the Heisenberg Hamiltonian converts to Eq. (2). Using supercells to estimate Heisenberg exchange parameters has a bottleneck due to periodic boundary conditions. The problem is that when we use a supercell, we can not calculate the exchange parameter for an aribritry distance. It is evident that we should restrict exchange parameter estimations within the supercell. If d_{ij} is the distance between atom i and atom j, then the supercell method restricts us to estimate only J_{ij} exchange parameters that $d_{ij} < L$, where L is supercell size. In the first-principles *ab initio* research, people consider this limitation. However, the problem is more challenging than it seems. In the following, we will explain it. According to Eq. (2), for each magnetic configuration, such as configuration k, we have a set of coefficients represented as α_{ki}. Using these coefficients, we build a coefficient matrix ($\mathbf{A}_{ki} = \alpha_{ki}$) to check the dependency of these matrix columns.

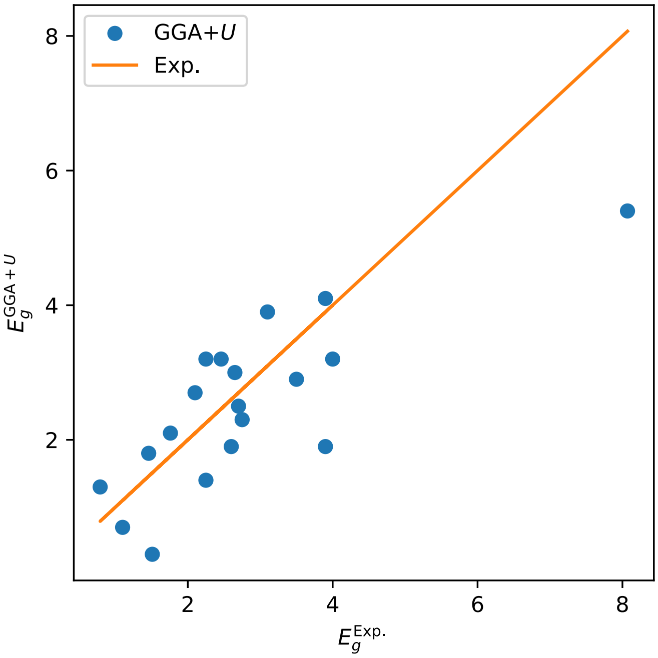

FIG. 3. Comparison of GGA+U band gap ($E_g^{\mathrm{GGA}+U}$) with experimental values ($E_g^{\mathrm{Expt.}}$).

If column i depends on others, we should restrict our method to calculate the exchange parameter up to $(i-1)$th nearest neighbor. In linear algebra, by considering kernel (or null) space, the dependency of columns of a matrix releases. The following equation defines the null space of matrix $\mathbf{A}$:

$$\mathrm{Ker}(\mathbf{A}) = \{\mathbf{x} : \mathbf{A}\mathbf{x} = \mathbf{0}\} = \mathrm{Null}(\mathbf{A}). \tag{B1}$$

The null space contains solutions for equation $\mathbf{A}\mathbf{x} = \mathbf{0}$. For a matrix with no-zero $\mathbf{x}$ solution, it means matrix columns are not independent. To shed light on the issue, we explain it using the NiO example. For a 2 × 2 × 2 supercell from NiO primitive cell (i.e., a trigonal), the matrix of coefficients for 12 (random) different configurations is

$$\begin{bmatrix} 96 & 48 & 192 & 96 & 192 & 64 & 384 & 48 & 288 \\ -16 & 0 & 0 & 0 & 32 & 0 & 0 & -48 & 16 \\ -32 & 48 & -64 & 96 & -64 & 64 & -128 & 48 & -96 \\ 16 & 0 & 48 & 48 & 64 & 0 & 96 & 0 & 80 \\ 8 & 12 & -8 & 48 & -32 & 16 & -16 & 0 & -24 \\ 0 & 12 & -24 & 60 & -48 & 16 & -48 & 12 & -48 \\ -8 & 12 & -8 & 48 & 0 & 16 & -16 & 0 & -8 \\ -8 & 0 & 8 & 24 & 32 & 0 & 16 & -24 & 24 \\ 8 & 24 & 24 & 72 & 32 & 32 & 48 & 24 & 40 \\ 24 & 36 & 48 & 84 & 48 & 48 & 96 & 36 & 72 \\ 28 & 24 & 64 & 60 & 72 & 32 & 128 & 12 & 100 \\ 48 & 36 & 96 & 72 & 96 & 48 & 192 & 24 & 144 \end{bmatrix}. \tag{B2}$$

The null space of the matrix $\mathbf{A}$ is as follows (by using null-space method in SCIPY.LINALG library of Python):

$$\mathbf{x} = \begin{bmatrix} 2 \\ 0 \\ -2 \\ 0 \\ 1 \\ 0 \\ 0 \\ 0 \\ 0 \end{bmatrix}, \begin{bmatrix} 0 \\ -4/3 \\ 0 \\ 0 \\ 0 \\ 1 \\ 0 \\ 0 \\ 0 \end{bmatrix}, \begin{bmatrix} 0 \\ 0 \\ -2 \\ 0 \\ 0 \\ 0 \\ 1 \\ 0 \\ 0 \end{bmatrix}, \begin{bmatrix} 1 \\ 0 \\ -2 \\ 0 \\ 0 \\ 0 \\ 0 \\ 0 \\ 1 \end{bmatrix}.$$

The first null-space solution, for example, tells us that coefficients in column 5 depend on columns 1 and 3 by the following equation:

$$2 \times \begin{bmatrix} 96 \\ -16 \\ -32 \\ 16 \\ 8 \\ 0 \\ -8 \\ -8 \\ 8 \\ 24 \\ 28 \\ 48 \end{bmatrix} - 2 \times \begin{bmatrix} 192 \\ 0 \\ -64 \\ 48 \\ -8 \\ -24 \\ -8 \\ 8 \\ 24 \\ 48 \\ 64 \\ 96 \end{bmatrix} + 1 \times \begin{bmatrix} 192 \\ 32 \\ -64 \\ 64 \\ -32 \\ -48 \\ 0 \\ 32 \\ 32 \\ 48 \\ 72 \\ 96 \end{bmatrix} = \begin{bmatrix} 0 \\ 0 \\ 0 \\ 0 \\ 0 \\ 0 \\ 0 \\ 0 \\ 0 \\ 0 \\ 0 \\ 0 \end{bmatrix}.$$

For 2 × 2 × 2 supercell, the supercell size apparently allows us to calculate J_i until the 12th nearest neighbor (using $d_{ij} < L$ criterion), however, null-space analysis warning us to restrict the calculation up to the 4th nearest neighbor. We should increase the supercell size to obtain exchange parameters beyond 4th nearest neighbor. For example, if we use 3 × 3 × 3 supercell for NiO, the matrix coefficient for 12 (random)

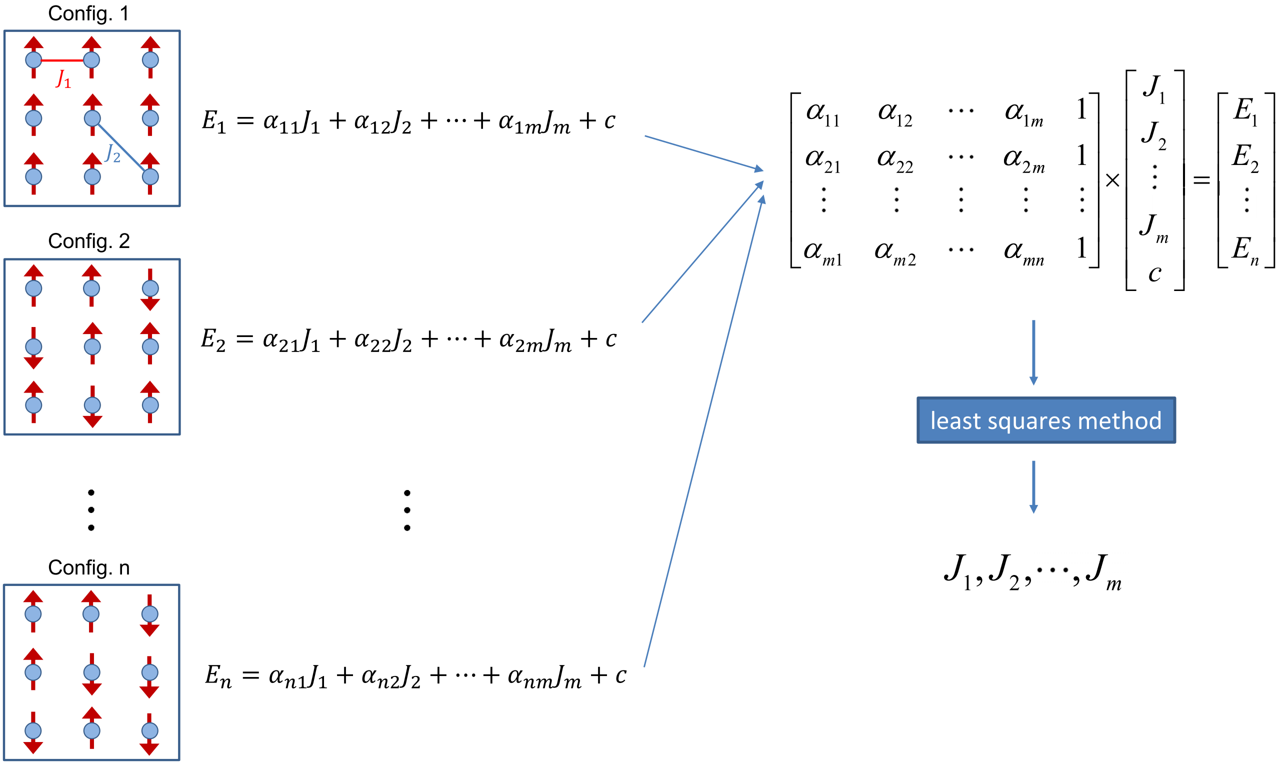

FIG. 4. The sketch illustrates the least-squares method to obtain Heisenberg exchanges. For each collinear magnetic configuration, the total energy of DFT consists of the Heisenberg exchange interactions between magnetic moments plus a constant due to other interactions. So using different configurations and the least-squares method, we can obtain exchange parameters.

different configurations is as follows:

$$\begin{bmatrix} 96 & 48 & 192 & 96 & 192 & 64 & 384 & 48 & 288 \\ -16 & 0 & 0 & 0 & 32 & 0 & 0 & -48 & 16 \\ -32 & 48 & -64 & 96 & -64 & 64 & -128 & 48 & -96 \\ 16 & 0 & 48 & 48 & 64 & 0 & 96 & 0 & 80 \\ 8 & 12 & -8 & 48 & -32 & 16 & -16 & 0 & -24 \\ 0 & 12 & -24 & 60 & -48 & 16 & -48 & 12 & -48 \\ -8 & 12 & -8 & 48 & 0 & 16 & -16 & 0 & -8 \\ -8 & 0 & 8 & 24 & 32 & 0 & 16 & -24 & 24 \\ 8 & 24 & 24 & 72 & 32 & 32 & 48 & 24 & 40 \\ 24 & 36 & 48 & 84 & 48 & 48 & 96 & 36 & 72 \\ 28 & 24 & 64 & 60 & 72 & 32 & 128 & 12 & 100 \\ 48 & 36 & 96 & 72 & 96 & 48 & 192 & 24 & 144 \end{bmatrix}. \tag{B3}$$

The null space of the matrix is

$$\mathbf{x} = \begin{bmatrix} 0 \\ 1 \\ 0 \\ 0 \\ -1/2 \\ 0 \\ 0 \\ 1 \\ 0 \end{bmatrix}.$$

Thus, we can obtain exchange parameters up to the 8th nearest neighbor (since column eight depends on column two and column five).

APPENDIX C: TRANSITION TEMPERATURE

To determine the transition temperature (T_C) for all compounds, we employ classical Monte Carlo (MC) simulations. We provide transition temperatures for all compounds along with Heisenberg exchange parameters for GGA and GGA+U approximations in Tables S5, S6, S7, and S8 of the Supplemental Material [56].

TABLE IV. The transition temperature for all samples was obtained using the Heisenberg exchange interactions calculated from the GGA+U method. T_{MC} was determined through Monte Carlo (MC) simulations. The transition temperature, denoted as T^*_{MC}, was then obtained by multiplying the Monte Carlo results with the $\frac{(S+1)}{S}$ factor. Additionally, $T_{\mathrm{Expt.}}$ represents the experimentally reported temperature.

Sample	S	T_{MC} (K)	T^*_{MC} (K)	$T_{\mathrm{Expt.}}$ (K)
NiO	1	220	440	523 [62]
MnO	$\frac{5}{2}$	26	36.4	117 [63]
MnS	$\frac{5}{2}$	54	75.6	152 [31]
MnSe	$\frac{5}{2}$	25	35	124 [64]
Cr_2O_3	$\frac{3}{2}$	118	195.8	308 [89]
Fe_2O_3	$\frac{5}{2}$	701	981.4	960 [89]
$BiFeO_3$	$\frac{5}{2}$	466	652.4	650 [90]
$NiBr_2$	1	19	38	52 [35]
YVO_3	$\frac{3}{2}$	49.2	81.6	77 [91]
$LiMnPO_4$	$\frac{5}{2}$	25	35	34–36 [92]
$LiNiPO_4$	1	11	22	21.8 [93]
$LiCoPO_4$	$\frac{3}{2}$	14	23.2	22–24 [92]
$YFeO_3$	$\frac{5}{2}$	469	656.6	644.5 [94]
$LaFeO_3$	$\frac{5}{2}$	527	737.8	750 [95]
$LiMnO_2$	2	111	166.5	300 [96]
$CrCl_2$	2	2	3	11.3–16 [68]
$KNiPO_4$	1	9	18	25 [21]
MnF_2	$\frac{5}{2}$	57	79.8	67.3 [66]
NiF_2	1	37	74	68.5 [65]
Fe_2TeO_6	$\frac{5}{2}$	351	491.4	210 [97]
La_2NiO_4	1	209	418	650 [98]
Cr_2TeO_6	$\frac{3}{2}$	17	28.2	93 [99]
KMnSb	$\frac{5}{2}$	217	303.8	237 [100]
Cr_2WO_6	$\frac{3}{2}$	28	46.4	45 [99]
$NiWO_4$	1	21	42	62 [101]
$MnWO_4$	$\frac{5}{2}$	20	28	8–13.5 [102]
$CoWO_4$	$\frac{3}{2}$	17	28.2	40 [103]
Li_2MnO_3	$\frac{3}{2}$	81	134.4	36.5 [104]
MnTe	$\frac{5}{2}$	189	264.6	310 [67]
MAPE		53%	44%	

TABLE V. The transition temperature for 18 samples was obtained using the Heisenberg exchange interactions calculated from the GGA+$U+V$ method. T_{MC} was determined through Monte Carlo (MC) simulations. The transition temperature, denoted as T^*_{MC}, was then obtained by multiplying the Monte Carlo results with the $\frac{(S+1)}{S}$ factor. Additionally, $T_{\mathrm{Expt.}}$ represents the experimentally reported temperature.

Sample	S	T_{MC} (K)	T^*_{MC} (K)	$T_{\mathrm{Expt.}}$ (K)
NiO	1	246	492	523 [62]
MnO	$\frac{5}{2}$	43	60.2	117 [63]
MnS	$\frac{5}{2}$	60	84	152 [31]
MnSe	$\frac{5}{2}$	26	36.4	124 [64]
Cr_2O_3	$\frac{3}{2}$	119	178.5	308 [89]
Fe_2O_3	$\frac{5}{2}$	804	1125.6	960 [89]
$BiFeO_3$	$\frac{5}{2}$	496	694.4	650 [90]
$LiMnPO_4$	$\frac{5}{2}$	28	39.2	34-36 [92]
$YFeO_3$	$\frac{5}{2}$	518	725.2	644.5 [94]
$LaFeO_3$	$\frac{5}{2}$	553	774.2	750 [95]
$LiMnO_2$	2	129	193.5	300 [96]
$CrCl_2$	2	2	3	11.3–16 [68]
MnF_2	$\frac{5}{2}$	72	100.8	67.3 [66]
NiF_2	1	47	94	68.5 [65]
$NiWO_4$	1	24	84	62 [101]
$MnWO_4$	$\frac{5}{2}$	28	39.2	8–13.5 [102]
$CoWO_4$	$\frac{3}{2}$	20	32	40 [103]
MnTe	$\frac{5}{2}$	196	274.4	310 [67]
MAPE		50%	43%	

In Table IV, you can find the transition temperature estimates (T_C^{MC}) for all 29 compounds obtained through MC simulations using the GGA+U results. Additionally, we include the T_C^{MC} correction ($T_C^{\mathrm{MC}*}$) by multiplying it by the factor $(S+1)/S$. Furthermore, in Table V, we present the transition temperatures for 18 compounds using the GGA+U+V approximation. It is important to note that the results obtained with the GGA+U+V approach are comparable to those of GGA+U and do not lead to an improved estimation of the transition temperature.

---

[1] D. Jiles, Recent advances and future directions in magnetic materials, Acta Mater. **51**, 5907 (2003).

[2] A. V. Kimel and M. Li, Writing magnetic memory with ultrashort light pulses, Nat. Rev. Mater. **4**, 189 (2019).

[3] T. Mori and S. Priya, Materials for energy harvesting: At the forefront of a new wave, MRS Bull. **43**, 176 (2018).

[4] R. J. Harrison, Neutron diffraction of magnetic materials, Rev. Mineral. Geochem. **63**, 113 (2006).

[5] A. R. Oganov and C. W. Glass, Crystal structure prediction using *ab initio* evolutionary techniques: Principles and applications, J. Chem. Phys. **124**, 244704 (2006).

[6] H. Zhang, High-throughput design of magnetic materials, Electron. Struct. **3**, 033001 (2021).

[7] A. Georges, G. Kotliar, W. Krauth, and M. J. Rozenberg, Dynamical mean-field theory of strongly correlated fermion systems and the limit of infinite dimensions, Rev. Mod. Phys. **68**, 13 (1996).

[8] W. M. C. Foulkes, L. Mitas, R. J. Needs, and G. Rajagopal, Quantum Monte Carlo simulations of solids, Rev. Mod. Phys. **73**, 33 (2001).

[9] R. J. Needs, M. D. Towler, N. D. Drummond, and P. L. Ríos, Continuum variational and diffusion quantum Monte Carlo calculations, J. Phys.: Condens. Matter **22**, 023201 (2010).

[10] V. I. Anisimov, J. Zaanen, and O. K. Andersen, Band theory and Mott insulators: Hubbard U instead of Stoner I, Phys. Rev. B **44**, 943 (1991).

[11] V. I. Anisimov, F. Aryasetiawan, and A. I. Lichtenstein, First-principles calculations of the electronic structure and spectra of strongly correlated systems: the LDA+U method, J. Phys.: Condens. Matter **9**, 767 (1997).

[12] R. Widita, S. Muhammady, R. D. Prasetiyawati, R. Marlina, L. Suryanegara, B. Purnama, R. Kurniadi, and Y. Darma, Revisiting the structural, electronic, and magnetic properties of (LaO)MnAs: Effect of hubbard correction and origin of Mott-insulating behavior, ACS Omega **6**, 4440 (2021).

[13] S. Sharma, E. K. U. Gross, A. Sanna, and J. K. Dewhurst, Source-free exchange-correlation magnetic fields in density functional theory, J. Chem. Theory Comput. **14**, 1247 (2018).

[14] S. M. Selbach, M.-A. Einarsrud, T. Tybell, and T. Grande, Synthesis of $BiFeO_3$ by wet chemical methods, J. Am. Ceram. Soc. **90**, 3430 (2007).

[15] F. Ahmadi, M. Rahimi-Nasrabadi, A. Fosooni, and M. Daneshmand, Synthesis and application of $CoWO_4$ nanoparticles for degradation of methyl orange, J. Mater. Sci.: Mater. Electron. **27**, 9514 (2016).

[16] T. Larbi, B. Ouni, A. Gantassi, K. Doll, M. Amlouk, and T. Manoubi, Structural, optical and vibrational properties of Cr_2O_3 with ferromagnetic and antiferromagnetic order: A combined experimental and density functional theory study, J. Magn. Magn. Mater. **444**, 16 (2017).

[17] W. Kunnmann, S. La Placa, L. Corliss, J. Hastings, and E. Banks, Magnetic structures of the ordered trirutiles Cr_2WO_6, Cr_2TeO_6 and Fe_2TeO_6, J. Phys. Chem. Solids **29**, 1359 (1968).

[18] M. Hagiwara and K. Katsumata, Magnetic properties of anhydrous $CrCl_2$, J. Magn. Magn. Mater. **140**, 1665 (1995).

[19] S. Navale, D. Bandgar, S. Nalage, G. Khuspe, M. Chougule, Y. Kolekar, S. Sen, and V. Patil, Synthesis of Fe_2O_3 nanoparticles for nitrogen dioxide gas sensing applications, Ceram. Int. **39**, 6453 (2013).

[20] F. Schucht, A. Dascoulidou, R. Müller, W. Jung, H.-U. Schuster, W. Bronger, and P. Müller, Die magnetischen eigenschaften der alkalimetall-manganpnictide KMnP, RbMnP, CsMnP, RbMnAs, KMnSb, KMnBi, RbMnBi und CsMnBi–neutronenbeugungsuntersuchungen und suszeptibilitätsmessungen, Z. anorg. allg. Chem. **625**, 31 (1999).

[21] M. Lujan, J.-P. Rivera, S. Kizhaev, H. Schmid, G. Triscone, J. Muller, Z.-G. Ye, B. Mettout, and R. Bouzerar, Magnetic measurements and magnetoelectric effect of pyroelectric $KNiPO_4$ single crystals, Ferroelectrics **161**, 77 (1994).

[22] N. Zhou, G. Chen, H. Zhang, and C. Zhou, Synthesis and transport properties of La_2NiO_4, Phys. B: Condens. Matter **404**, 4150 (2009).

[23] M. Idrees, M. Nadeem, M. Shah, and T. Shin, Anomalous octahedral distortions in $LaFe_{1-x}Ni_xO_3$, J. Phys. D: Appl. Phys. **44**, 455303 (2011).

[24] P. Strobel and B. Lambert-Andron, Crystallographic and magnetic structure of Li_2MnO_3, J. Solid State Chem. **75**, 90 (1988).

[25] R. Newnham and M. Redman, Crystallographic data for $LiMgPO_4$, $LiCoPO_4$, and $LiNiPO_4$, J. Am. Ceram. Soc. **48**, 547 (1965).

[26] V. Galakhov, M. Korotin, N. Ovechkina, E. Kurmaev, V. Gorshkov, D. Kellerman, S. Bartkowski, and M. Neumann, Electronic structure of LiMnO: X-ray emission and photoelectron spectra and band structure calculations, Eur. Phys. J. B **14**, 281 (2000).

[27] S. Geller and J. Durand, Refinement of the structure of $LiMnO_4$, Acta Crystallogr. **13**, 325 (1960).

[28] I. Abrahams and K. Easson, Structure of lithium nickel phosphate, Acta Crystallogr C: Cryst. Struct. Commun. **49**, 925 (1993).

[29] X. Li, J. Lu, G. Peng, L. Jin, and S. Wei, Solvothermal synthesis of MnF_2 nanocrystals and the first-principle study of its electronic structure, J. Phys. Chem. Solids **70**, 609 (2009).

[30] F. Tran, P. Blaha, K. Schwarz, and P. Novák, Hybrid exchange-correlation energy functionals for strongly correlated electrons: Applications to transition-metal monoxides, Phys. Rev. B **74**, 155108 (2006).

[31] J. K. Clark, V. Yannello, A. M. Samarakoon, C. Ross, M. C. Uible, V. O. Garlea, and M. Shatruk, Inelastic neutron scattering study of magnetic exchange pathways in MnS, J. Phys. Chem. C **125**, 16183 (2021).

[32] Q. Peng, Y. Dong, Z. Deng, H. Kou, S. Gao, and Y. Li, Selective synthesis and magnetic properties of α-MnSe and $MnSe_2$ uniform microcrystals, J. Phys. Chem. B **106**, 9261 (2002).

[33] C. Reig, V. Munoz, C. Gomez, C. Ferrer, and A. Segura, Growth and characterisation of MnTe crystals, J. Cryst. Growth **223**, 349 (2001).

[34] S. Saranya, S. Senthilkumar, K. V. Sankar, and R. K. Selvan, Synthesis of $MnWO_4$ nanorods and its electrical and electrochemical properties, J. Electroceram. **28**, 220 (2012).

[35] P. Day, A. Dinsdale, E. Krausz, and D. Robbins, Optical and neutron diffraction study of the magnetic phase diagram of $NiBr_2$, J. Phys. C: Solid State Phys. **9**, 2481 (1976).

[36] M. Costa, J. Paixao, M. De Almeida, and L. Andrade, Charge densities of two rutile structures: NiF_2 and CoF_2, Acta Crystallogr B: Struct. Sci. **49**, 591 (1993).

[37] R. O. Keeling, The structure of $NiWo_4$, Acta Crystallogr. **10**, 209 (1957).

[38] A. Racu, D. H. Ursu, O. Kuliukova, C. Logofatu, A. Leca, and M. Miclau, Direct low temperature hydrothermal synthesis of $YFeO_3$ microcrystals, Mater. Lett. **140**, 107 (2015).

[39] G. Herrera, E. Chavira, J. Jimenez-Mier, L. Banos, J. Guzmán, and C. Flores, Synthesis and structural characterization of YVO_3 prepared by sol–gel acrylamide polymerization and solid state reaction methods, J. Sol-Gel Sci. Technology **46**, 1 (2008).

[40] P. Giannozzi, S. Baroni, N. Bonini, M. Calandra, R. Car, C. Cavazzoni, D. Ceresoli, G. L. Chiarotti, M. Cococcioni, I. Dabo, A. D. Corso, S. de Gironcoli, S. Fabris, G. Fratesi, R. Gebauer, U. Gerstmann, C. Gougoussis, A. Kokalj, M. Lazzeri, L. Martin-Samos *et al.*, Quantum espresso: A modular and open-source software project for quantum simulations of materials, J. Phys.: Condens. Matter **21**, 395502 (2009).

[41] K. Koepernik and H. Eschrig, Full-potential nonorthogonal local-orbital minimum-basis band-structure scheme, Phys. Rev. B **59**, 1743 (1999).

[42] K. F. Garrity, J. W. Bennett, K. M. Rabe, and D. Vanderbilt, Pseudopotentials for high-throughput DFT calculations, Comput. Mater. Sci. **81**, 446 (2014).

[43] H. J. Monkhorst and J. D. Pack, Special points for brillouin-zone integrations, Phys. Rev. B **13**, 5188 (1976).

[44] M. Cococcioni and S. de Gironcoli, Linear response approach to the calculation of the effective interaction parameters in the LDA + U method, Phys. Rev. B **71**, 035105 (2005).

[45] I. Timrov, N. Marzari, and M. Cococcioni, Hubbard parameters from density-functional perturbation theory, Phys. Rev. B **98**, 085127 (2018).

[46] I. Timrov, N. Marzari, and M. Cococcioni, Self-consistent hubbard parameters from density-functional perturbation theory in the ultrasoft and projector-augmented wave formulations, Phys. Rev. B **103**, 045141 (2021).

[47] G. Henkelman, A. Arnaldsson, and H. Jónsson, A fast and robust algorithm for bader decomposition of charge density, Comput. Mater. Sci. **36**, 354 (2006).

[48] E. Sanville, S. D. Kenny, R. Smith, and G. Henkelman, Improved grid-based algorithm for bader charge allocation, J. Comput. Chem. **28**, 899 (2007).

[49] W. Tang, E. Sanville, and G. Henkelman, A grid-based bader analysis algorithm without lattice bias, J. Phys.: Condens. Matter **21**, 084204 (2009).

[50] M. Yu and D. R. Trinkle, Accurate and efficient algorithm for Bader charge integration, J. Chem. Phys. **134**, (2011).

[51] W. Cheney and D. Kincaid, *Linear Algebra: Theory and Applications* (Jones & Bartlett Learning, Burlington, MA, 2012).

[52] M. Alaei and H. Karimi, A deep investigation of NiO and MnO through the first principle calculations and Monte Carlo simulations, Electron. Struct. **5**, 025001 (2023).

[53] N. Rezaei, M. Alaei, and H. Akbarzadeh, ESpinS: A program for classical Monte-Carlo simulations of spin systems, Comput. Mater. Sci. **202**, 110947 (2022).

[54] J. T. Krogel, J. A. Santana, and F. A. Reboredo, Pseudopotentials for quantum Monte Carlo studies of transition metal oxides, Phys. Rev. B **93**, 075143 (2016).

[55] X. Xu and D. G. Truhlar, Performance of effective core potentials for density functional calculations on 3D transition metals, J. Chem. Theory Comput. **8**, 80 (2012).

[56] See Supplemental Material at http://link.aps.org/supplemental/10.1103/PhysRevB.108.144413 for the projected density of states (PDOS) of each compound using the GGA+U method, and Heisenberg exchange parameters from DFT calculations based on Quantum-Espresso (using GGA and GGA+U) and FPLO (using GGA) codes for each compound.

[57] S. Lee, S. Choi, J. Kim, H. Sim, C. Won, S. Lee, S. A. Kim, N. Hur, and J.-G. Park, Antiferromagnetic ordering in Li_2MnO_3 single crystals with a two-dimensional honeycomb lattice, J. Phys.: Condens. Matter **24**, 456004 (2012).

[58] D. M. Korotin, V. V. Mazurenko, V. I. Anisimov, and S. V. Streltsov, Calculation of exchange constants of the Heisenberg model in plane-wave-based methods using the Green's function approach, Phys. Rev. B **91**, 224405 (2015).

[59] V. L. Campo and M. Cococcioni, Extended DFT+U+V method with on-site and inter-site electronic interactions, J. Phys.: Condens. Matter **22**, 055602 (2010).

[60] B. Himmetoglu, A. Floris, S. de Gironcoli, and M. Cococcioni, Hubbard-corrected dft energy functionals: The LDA+U description of correlated systems, Int. J. Quantum Chem. **114**, 14 (2014).

[61] M. Cococcioni and N. Marzari, Energetics and cathode voltages of LimPO$_4$ olivines (m = Fe, Mn) from extended hubbard functionals, Phys. Rev. Mater. **3**, 033801 (2019).

[62] M. T. Hutchings and E. Samuelsen, Measurement of spin-wave dispersion in NiO by inelastic neutron scattering and its relation to magnetic properties, Phys. Rev. B **6**, 3447 (1972).

[63] M. Kohgi, Y. Ishikawa, and Y. Endoh, Inelastic neutron scattering study of spin waves in MnO, Solid State Commun. **11**, 391 (1972).

[64] A. Milutinović, N. Tomić, S. Dević, P. Milutinović, and Z. V. Popović, Raman scattering by spin excitations in α-MnSe, Phys. Rev. B **66**, 012302 (2002).

[65] P. A. Fleury, Paramagnetic spin waves and correlation functions in NiF_2, Phys. Rev. **180**, 591 (1969).

[66] P. Nordblad, L. Lundgren, E. Figueroa, and O. Beckman, Specific heat and magnetic susceptibility of MnF_2 and $Mn_{0.98}Fe_{0.02}F_2$ near Tn, J. Magn. Magn. Mater. **23**, 333 (1981).

[67] W. Szuszkiewicz, E. Dynowska, B. Witkowska, and B. Hennion, Spin-wave measurements on hexagonal MnTe of NiAs-type structure by inelastic neutron scattering, Phys. Rev. B **73**, 104403 (2006).

[68] M. Winkelmann, M. Baehr, M. Reehuis, M. Steiner, M. Hagiwara, and K. Katsumata, Structural and magnetic characterization of a new phase of $CrCl_2$, J. Phys. Chem. Solids **58**, 481 (1997).

[69] R. F. Bader, Atoms in molecules, Acc. Chem. Res. **18**, 9 (1985).

[70] A. Arnaldsson, W. Tang, S. Chill, W. Chai, R. Anselm, and G. Henkelman, Bader Charge Analysis (2020), version 1.04.

[71] S. Das, M. Bhuyan, and M. Basith, First-principles calculation of the electronic and optical properties of Gd_2FeCrO_6 double perovskite: Effect of Hubbard u parameter, J. Mater. Res. Technol. **13**, 2408 (2021).

[72] R. Tesch and P. M. Kowalski, Hubbard u parameters for transition metals from first principles, Phys. Rev. B **105**, 195153 (2022).

[73] J. W. Bennett, B. G. Hudson, I. K. Metz, D. Liang, S. Spurgeon, Q. Cui, and S. E. Mason, A systematic determination of Hubbard U using the GBRV ultrasoft pseudopotential set, Comput. Mater. Sci. **170**, 109137 (2019).

[74] S. Youn, B. Min, and A. J. Freeman, Crossroads electronic structure of MnS, MnSe, and MnTe, Phys. Status Solidi B **241**, 1411 (2004).

[75] J. Singh, V. Verma, R. Kumar, S. Sharma, and R. Kumar, Effect of structural and thermal disorder on the optical band gap energy of Cr_2O_3 nanoparticles, Mater. Res. Express **6**, 085039 (2019).

[76] S. Piccinin, The band structure and optical absorption of hematite (α-Fe_2O_3): A first-principles Gw-BsE study, Phys. Chem. Chem. Phys. **21**, 2957 (2019).

[77] K. A. McDonnell, N. Wadnerkar, N. J. English, M. Rahman, and D. Dowling, Photo-active and optical properties of bismuth ferrite ($BiFeO_3$): An experimental and theoretical study, Chem. Phys. Lett. **572**, 78 (2013).

[78] F. Zhou, K. Kang, T. Maxisch, G. Ceder, and D. Morgan, The electronic structure and band gap of $LiFePO_4$ and $LiMnPO_4$, Solid State Commun. **132**, 181 (2004).

[79] M. Wang and T. Wang, Structural, magnetic and optical properties of Gd and Co Co-doped $YFeO_3$ nanopowders, Materials **12**, 2423 (2019).

[80] I. W. Boateng, R. Tia, E. Adei, N. Y. Dzade, C. R. A. Catlow, and N. H. De Leeuw, A DFT+U investigation of hydrogen adsorption on the $LaFeO_3$ (010) surface, Phys. Chem. Chem. Phys. **19**, 7399 (2017).

[81] Z.-F. Huang, C.-Z. Wang, X. Meng, Y. Sun, and G. Chen, Competition between ferromagnetic and antiferromagnetic interaction in monoclinic $LiMnO_2$, Comput. Mater. Sci. **42**, 504 (2008).

[82] S. Arumugam, P. Sivaprakash, A. Dixit, R. Chaurasiya, L. Govindaraj, M. Sathiskumar, S. Chatterjee, and R. Suryanarayanan, Complex magnetic structure and magnetocapacitance response in a non-oxide NiF_2 system, Sci. Rep. **9**, 3200 (2019).

[83] G. Behera, Structural, magnetic and dielectric investigation of iron tellurate Fe_2TeO_6, Master Thesis, Department of Physics & Astronomy, National Institute of Technology Rourkela, India, Rourkela (2016).

[84] R. Laouici, S. Douafer, H. Lahmar, G. Rekhila, M. Trari, and M. Benamira, Elaboration and studies of physical and photoelectrochemical properties of La_2NiO_4 and its use with SnO_2 in photo-evolution of hydrogen under visible light irradiation, Optik **236**, 166654 (2021).

[85] S. Shepard and M. Smeu, *Ab initio* study of structural and electronic properties of copper and nickel tungstate, Comput. Mater. Sci. **143**, 301 (2018).

[86] J. C. Peixoto, A. E. Nogueira, A. Dias, J. A. Torres, J. C. da Cruz, C. Ribeiro, and K. P. Siqueira, Experimental evaluation of the activity and selectivity of pure $MnWO_4$ and doped with rare earth ions in the Co_2 photoreduction process, Mater. Res. Bull. **153**, 111912 (2022).

[87] E. Bandiello, P. Rodríguez-Hernández, A. Muñoz, M. B. Buenestado, C. Popescu, and D. Errandonea, Electronic properties and high-pressure behavior of wolframite-type $CoWO_4$, Mater. Adv. **2**, 5955 (2021).

[88] M. Ranjeh, M. Masjedi-Arani, M. Salavati-Niasari, and H. Moayedi, Edta-modified sol-gel synthesis of monoclinic Li_2MnO_3 nanoparticles as an effective photocatalyst for degradation of organic dyes, J. Mol. Liq. **300**, 112292 (2020).

[89] E. Samuelsen, M. Hutchings, and G. Shirane, Inelastic neutron scattering investigation of spin waves and magnetic interactions in Cr_2O_3, Physica (Amsterdam) **48**, 13 (1970).

[90] J. Park, S.-H. Lee, S. Lee, F. Gozzo, H. Kimura, Y. Noda, Y. Jai Choi, V. Kiryukhin, S.-W. Cheong, Y. Jo *et al.*, Magnetoelectric feedback among magnetic order, polarization, and lattice in multiferroic $BiFeO_3$, J. Phys. Soc. Jpn. **80**, 114714 (2011).

[91] L. Wang, T. Maxisch, and G. Ceder, Oxidation energies of transition metal oxides within the GGA+U framework, Phys. Rev. B **73**, 195107 (2006).

[92] S. Gnewuch and E. E. Rodriguez, Distinguishing the intrinsic antiferromagnetism in polycrystalline $LiCoPO_4$ and $LiMnPO_4$ olivines, Inorg. Chem. **59**, 5883 (2020).

[93] Y. N. Kharchenko, N. Kharcheno, M. Baran, and R. Szymczak, Weak ferromagnetism and an intermediate incommensurate antiferromagnetic phase in $LiNiPO_4$, Low Temp. Phys. **29**, 579 (2003).

[94] H. Shen, J. Xu, A. Wu, J. Zhao, and M. Shi, Magnetic and thermal properties of perovskite $YFeO_3$ single crystals, Mater. Sci. Eng. B **157**, 77 (2009).

[95] W. Koehler and E. Wollan, Neutron-diffraction study of the magnetic properties of perovskite-like compounds $LaBO_3$, J. Phys. Chem. Solids **2**, 100 (1957).

[96] D. Kellerman, J. Medvedeva, V. Gorshkov, A. Kurbakov, V. Zubkov, A. Tyutyunnik, and V. Trunov, Structural and magnetic properties of orthorhombic Li_xMnO_2, Solid State Sci. **9**, 196 (2007).

[97] S. Kaushik, B. Sahu, S. Mohapatra, and A. Singh, Structural, dielectric and magnetic studies of magnetoelectric trirutile Fe_2TeO_6, in *AIP Conference Proceedings*, Vol. 1731 (AIP Publishing, Melville, NY, 2016).

[98] G. H. Lander, P. J. Brown, J. Spal, and J. M. Honig, Structural and magnetization density studies of La_2NiO_4, Phys. Rev. B **40**, 4463 (1989).

[99] M. Zhu, M. Matsumoto, M. B. Stone, Z. L. Dun, H. D. Zhou, T. Hong, T. Zou, S. D. Mahanti, and X. Ke, Amplitude modes in three-dimensional spin dimers away from quantum critical point, Phys. Rev. Res. **1**, 033111 (2019).

[100] N. Mao, H. Wang, X. Hu, C. Niu, B. Huang, and Y. Dai, Antiferromagnetic topological insulator in stable exfoliated two-dimensional materials, Phys. Rev. B **102**, 115412 (2020).

[101] M. A. Prosnikov, V. Y. Davydov, A. N. Smirnov, M. P. Volkov, R. V. Pisarev, P. Becker, and L. Bohatý, Lattice and spin dynamics in a low-symmetry antiferromagnet $NiWO_4$, Phys. Rev. B **96**, 014428 (2017).

[102] G. Lautenschläger, H. Weitzel, T. Vogt, R. Hock, A. Böhm, M. Bonnet, and H. Fuess, Magnetic phase transitions of $MnWO_4$ studied by the use of neutron diffraction, Phys. Rev. B **48**, 6087 (1993).

[103] J. Deng, L. Chang, P. Wang, E. Zhang, J. Ma, and T. Wang, Preparation and magnetic properties of $CoWO_4$ nanocrystals, Cryst. Res. Technol. **47**, 1004 (2012).

[104] X. Zhang, S. Tang, and Y. Du, Synthesis and magnetic properties of antiferromagnetic Li_2MnO_3 nanoribbons, Phys. Lett. A **375**, 3196 (2011).